npj | 2D materials and applications

www.nature.com/npj2dmaterials

ARTICLE OPEN

Check for updates

Strain tuning MoO_3 vibrational and electronic properties

Sergio Puebla[1]✉, Hao Li[1], Onur Çakıroğlu[1], Estrella Sánchez-Viso[1], C. Munuera[1], Roberto D'Agosta[2,3]✉ and Andres Castellanos-Gomez[1]✉

This work investigates the vibrational and electrical properties of molybdenum trioxide (α-MoO_3) upon tensile strain applied along different crystal directions. Using a three-point bending setup in combination with Raman spectroscopy, we report measurements of a blueshift of the Raman modes when uniaxial tensile strain is applied along the *a*- and *c*-axis to this material. Furthermore, the electrical measurements reveal an increase in resistance with strain applied along both in-plane directions. The findings from the uniaxial strain and Raman spectroscopy measurements are further confirmed by ab-initio calculations. This study provides valuable insights into the mechanical and vibrational properties of α-MoO_3 and its potential use in several applications. This study contributes to the growing body of knowledge on the properties of α-MoO_3 and lays the foundation for further exploration of its potential applications. Given MoO_3 holding the natural hyperbolic phonon polaritons, attracting significant research interest, this study has the potential to arouse the curiosity of the scientific community.

npj 2D Materials and Applications (2024)8:5 ; https://doi.org/10.1038/s41699-024-00442-3

INTRODUCTION

A variety of two-dimensional (2D) materials have been researched since the discovery of graphene in 2004[1] and some of their properties, like flexibility or charge carrier mobility, even surpasses those of their bulk counterparts[2,3]. Inorganic semiconducting 3D materials tend to break at moderate strain levels, which hampers their application in flexible electronics. 2D materials have the property of being durable when they encounter a mechanical deformation due to the lack of dangling bonds on the surface[4]. Along with it, these materials proved to have properties sensitive to deformations, due to the change of the band structure[5–9]. In recent years, strain engineering has become a useful technique to control different properties of the materials. There are different methods to apply strain such as lattice mismatch, pre-strained flexible substrates or bending flexible substrates, among others[3,10–14]. Amid the properties that change upon deformation, the phonon structure of the material is one of the most evident. This phonon shift with strain has been observed in a wide selection of van der Waals (vdW) materials, with either blue- and red-shift of the Raman modes[3,8,10–17]. Raman spectroscopy is a powerful and valuable technique for studying the phonons of a material, and it is widely used in scientific research[7,18–21]. By providing detailed information about the vibrational modes of atoms and molecules, it allows to explore the structural and chemical properties of materials with precision, versatility, and ease of use.

A broad spectrum of layered oxide materials has been thoroughly studied, such as TiO_2[22,23], ZnO[24–26], MnO_2[27–29], among others[30,31]. MoO_3 owns several crystal systems, being the alpha phase (α-MoO_3) the most thermodynamically stable with a wide bandgap larger than 2.7 eV[32]. This phase is formed by layered sheets in an orthorhombic system, belonging to the space group *Pbnm* (#62)[33–37], with lattice parameters are: $a = 3.96$ Å, $c = 3.72$ Å, $b = 13.86$ Å, belonging to the D_{2h}^{16} point group exhibiting in-plane anisotropic properties[38], providing a new degree of freedom in space when compared to isotropic materials that can be exploited in diverse ways[32]. The Fig. 1 shows a representation of the MoO_3 crystal structure using the *Pbnm* space group notation, panels (*a*-*c*) show the three axes views and, in the panel (d), a cavalier projection of the crystal structure. In the panel (e) is shown one octahedron from (d) naming the different oxygen atoms bonded to the molybdenum atom. α-MoO_3 is useful in emerging applications such as energy storage[39–41], nanoelectronics[42–44], gas sensors[45], supercapacitors[46,47], mechanical engineering[48,49], resistive memories[50], among others. Recently, MoO_3 has been deeply investigated since it possesses natural phonon polaritons, caused from its in-plane anisotropy[51–57]. Understanding and controlling the anisotropic material's properties, especially its response to mechanical strain, are crucial for optimizing its performance in these applications and make it broader, such as straintronics or flexible technologies[38].

In a previous work we studied the relation between the direction of the applied strain and the mechanical response of α-MoO_3 exfoliated flakes using buckling metrology method[38], while the current findings are certainly intriguing, it is clear that further investigations in this direction are necessary to fully understand the complexities at play. We have observed a scarcity of investigations into the anisotropic properties of molybdenum trioxide, thus this work will increase the comprehension of this material in terms of its vibrational and electrical properties related to the mechanical tensile strain along different crystal directions. We have carried out straining measurements with a homemade three-point bending set up (see ref. [58] for more information about this setup), applying uniaxial tensile strain while varying the orientation of the strain. We have combined this technique with Raman spectroscopy measurement observing, an unprecedent blueshift of different Raman modes when the strain is applied along the *a*- and *c*-axes of the α-MoO_3, unlike the majority of vdW materials studied so far, where Raman shifts are typically observed in the redshift direction upon the application of a tensile strain. Furthermore, we have performed, with the three-point bending setup, electrical measurements, observing an increase in

[1]Materials Science Factory, Instituto de Ciencia de Materiales de Madrid (ICMM-CSIC), Madrid E-28049, Spain. [2]Nano-Bio Spectroscopy Group and European Theoretical Spectroscopy Facility (ETSF), Departamento Polímeros y Materiales Avanzados: Física, Química y Tecnología, Universidad del País Vasco UPV/EHU, San Sebastián, Spain. [3]IKERBASQUE, Basque Foundation for Science, Bilbao, Spain. ✉email: Sergio.puebla@csic.es; roberto.dagosta@ehu.es; andres.castellanos@csic.es

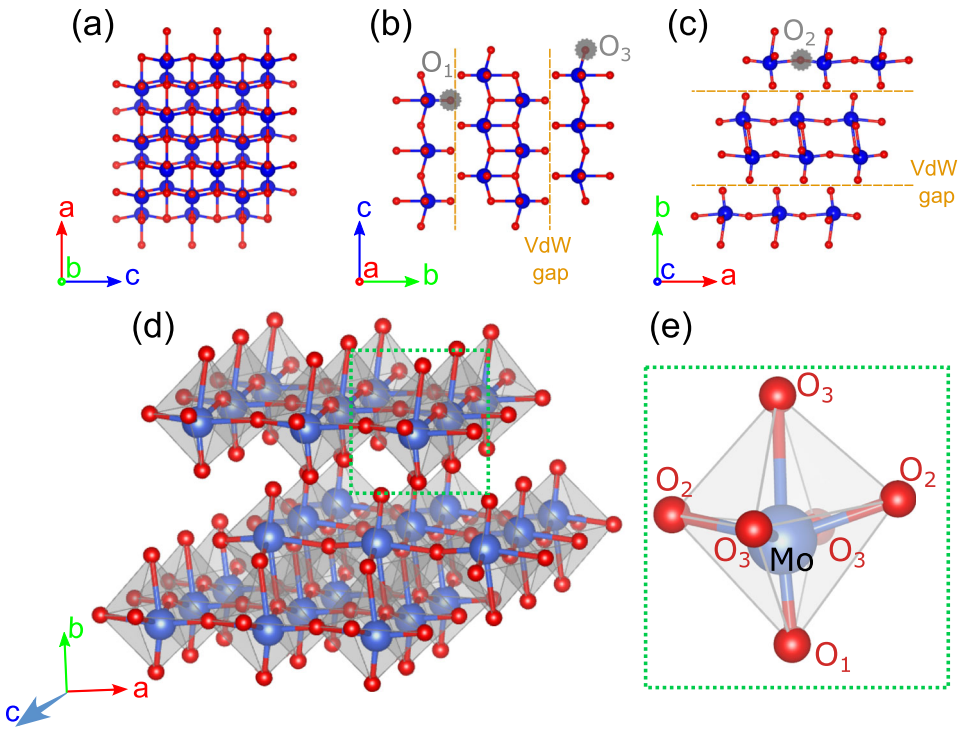

Fig. 1 Crystal structure representation of α-MoO_3 using *Pbnm* space group notation. Perpendicular to (**a**) *b*-axis, (**b**) *a*-axis and (**c**) *c*-axis. **d** Cavalier projection of the structure. **e** Zoom of the panel (**d**), Mo atom bonded with every O, showing its labels. The dark yellow dashed lines represent the layers gap.

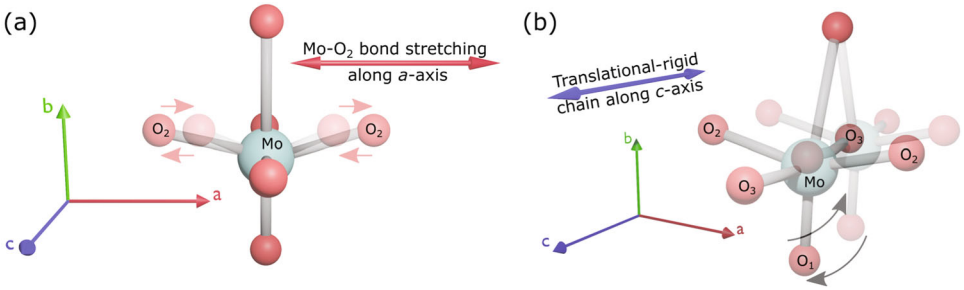

Fig. 2 A_g Raman modes belonging to α-MoO_3. a $A_g{}^a$ Raman mode belonging to the Mo-O_2 bond stretching along *a*-axis. **b** $A_g{}^c$ Raman mode belonging to translational vibration along *c*-axis. Labeling the oxygen atoms as in the Fig. 1. Note the translational and stretch movements are exaggerated to make a clearer explanation.

resistance when a tensile strain is applied along both in-plane directions. Moreover, we have performed ab initio calculations, supporting the findings of the energy shift of the Raman modes and the change in the electrical resistance observed in the experiments. These findings not only contribute to the fundamental understanding of the material but also have practical implications for the development of innovative devices and technologies.

RESULTS AND DISCUSSION

The growth of α-MoO_3 is carried out through a modified version of the physical vapor deposition technique, as described in the ref. [59], developed by Molina-Mendoza et al. In short, this process involves placing a molybdenum foil on a preheated hot plate at 540 °C and then positioning a SiO_2/Si wafer or a muscovite mica piece on top of the foil. The resulting α-MoO_3 flakes grown on the SiO_2/Si wafer tend to present a randomly oriented structure and a low surface-to-thickness ratio. On the other hand, the MoO_3 grown on the mica substrate exhibit wider films with a higher concentration of thinner and wider flakes. This difference is attributed to the mica surface (001) providing a defect-free target substrate, which allows for van der Waals (lattice matching relaxed) epitaxial growth of the MoO_3.

In order to study the Raman spectra taken in our measurements, we focus on two specific modes: The $A_g{}^c$ mode, which corresponds to the translation vibration of the rigid MoO_6 octahedra chains along the *c*-axis, and the $A_g{}^a$ mode, corresponding to the asymmetric stretching vibration of O-Mo-O atoms along the *a*-axis[35,37]. These specific modes are represented, exaggerating its displacements for a clearer understanding, in the Fig. 2.

For the study of the Raman modes we have used samples grown on both mica muscovite and a 300 nm SiO_2/Si wafer and then, by using a Gel-Film (Gel-Pak WF x4 6.0 mil) deterministic transfer methods (see ref. [60] for a detailed information) is used for transferring the flake on the polycarbonate (PC) substrate (Fig. 3a depicts a picture of a α-MoO_3 transferred, displaying its crystal orientation), which is then placed into a custom-built three-point

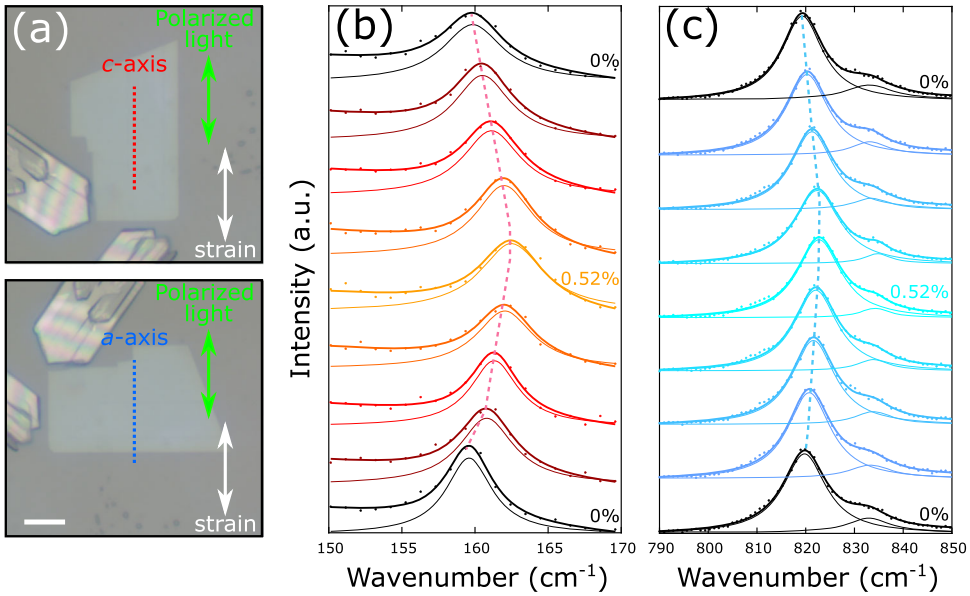

Fig. 3 Raman shift of A_g^c and A_g^a modes in MoO_3 when applying strain along *c* and *a*-axes, respectively. a Optical pictures of a α-MoO_3 sample placed on a polycarbonate substrate, showing with red dots the direction of the *c*-axis (top) and the orientation of the *a*-axis with blue dots (bottom). The strain applied and the direction of the linearly polarized laser used are shown in white and green arrows, respectively. Scale bar of 10 μm is shown in the bottom image. **b** The Raman shift of A_g^c mode when the strain and the polarization are set along the *c*-axis and (**c**) The Raman shift of A_g^a Raman mode when the strain and the polarization are set along the *a*-axis. Both measurements are taken along a full cycle of strain (from 0% to 0.52% to 0% again). The experimental data is plotted in dots, which is fitted with a pseudo-Voigt function, depicting the function with a thin line, and adding the background with a thicker one. To stress the shift of the modes, dashed light red and blue lines are added along the peaks as a guide for the eye in the (**b**) and (**c**) plots, respectively.

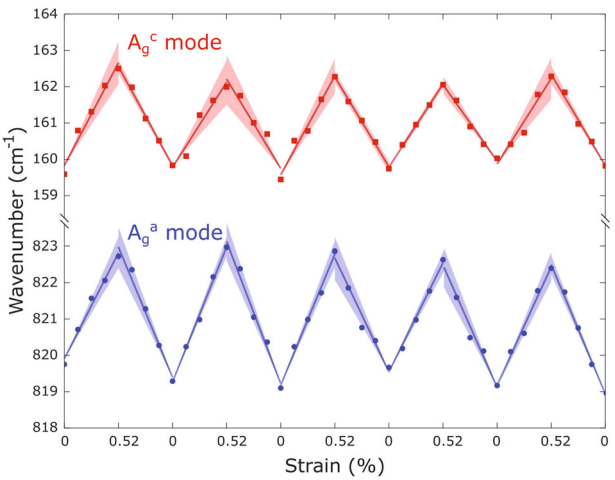

Fig. 4 A_g^c mode (in red) and A_g^a mode (in blue) of a α-MoO_3 sample along 5 cycles of strain. Experimental data is plotted as squares and dots, respectively. A linear fit of the data is used to extract the gauge factor, and the shaded area around the fit represents the uncertainty of the gauge factor extracted from the linear fit.

bending set up (see Supplementary Fig. 1) to apply strain along different in-plane directions as described in the ref. [9] The samples were subjected to a strain ranging from 0% to 0.52%, with a step of 0.13%, while taking polarized Raman spectra in each strain direction (For more detailed information on angle-resolved polarized Raman spectroscopy technique, we refer the reader to our previous work[38]). We decided to set that maximum value of strain due to we observed slippage in our samples for higher values, being 0.52% a safe maximum strain, Supplementary Fig. 2 shows the slippage behavior (observed in the work[61]) and Supplementary Fig. 3 optical microscope pictures of a tested sample before, and after the strain measurements are carried out, not observing new cracks and proving that the range we set is safe.

Panels (b) and (c) in Fig. 3 show the Raman spectra of MoO_3 flake upon a uniaxial tensile strain along the two perpendicular directions of the material, with the polarization set parallel to the strain, leads to a blueshift in the wavenumber of two significant Raman modes, the A_g^c mode (~160 cm^{-1}) and the A_g^a mode (~820 cm^{-1}), respectively. The shift in the wavenumber of these modes is a direct result of the change in the lattice structure of the MoO_3 flakes under the applied strain. When the samples were released from the strain, the wavenumbers of the Raman modes shifted back to their original values, indicating that the change in the lattice structure is reversible.

In order to test the reproducibility of these strain tuning Raman spectra, Fig. 4 shows the wavenumber shift of the A_g^c, painted in red colors, and A_g^a, shown in blue colors, modes along 5 cycles of loading/unloading (Supplementary Figs. 4 and 5 show the full Raman spectra of the cycles in Fig. 4). We have studied six samples using SiO_2 as the target substrate and three samples using mica. We then obtain a Raman Gauge Factor (RGF), defined as the shift of the wavenumber per % of tensile strain.

By applying strain along the *c*-axis we have encountered, for the A_g^c mode, an average value of 4.2 ± 0.7 cm^{-1}/% (3.7 ± 0.6 cm^{-1}/% for the samples belonging to the SiO_2 target substrate and 5.3 ± 1 cm^{-1}/% for the mica substrate ones), and for the A_g^a mode, an average value of -1.0 ± 0.9 cm^{-1}/% (-1.1 ± 0.6 cm^{-1}/% for the samples belonging to the SiO_2 target substrate and -0.4 ± 1.2 cm^{-1}/% for the mica substrate one).

By applying strain along the *a*-axis we have found for the A_g^a mode, an average value of 5.4 ± 1 cm^{-1}/% (5.3 ± 1 cm^{-1}/% for the samples belonging to the SiO_2 target substrate and 5.5 ± 0.9 cm^{-1}/% for the mica substrate one), and for the A_g^c mode, an average value of 1.8 ± 0.6 cm^{-1}/% (2.3 ± 0.5 cm^{-1}/% for the samples belonging to the SiO_2 target substrate and 1.6 ± 0.7 cm^{-1}/% for the mica substrate one).

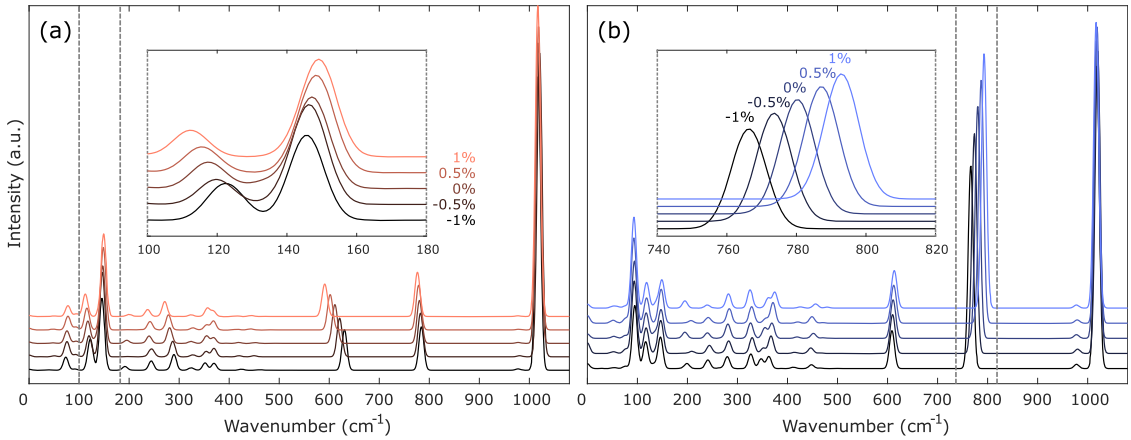

Fig. 5 Theoretical Raman shift of MoO_3 under strain. Theoretical Calculations of α-MoO_3 strained along (**a**) *c*-axis and (**b**) *a*-axis. It is shown a compression strain of −1% (in black color in both plots), to a tensile strain of +1% in red for the *c*-axis and blue for the *a*-axis. An inset of the plot is used to focus the attention of the A_g^c (with a range of 100–180 cm^{-1}) and A_g^a (with a range of 740–820 cm^{-1}), respectively.

Supplementary Table 1 of the Supplementary Information shows the average values of the RGF of each sample along with its uncertainty, and thickness, ranging from 16 nm to 23 nm. (An AFM image of one of the samples tested is displayed in Supplementary Fig. 6). In this table, the RGF values are presented with polarization parallel to the direction of the applied strain, except in the cells where the direction of polarization is specified as "polar. // *c*" or "polar. // *a*". When applying strain along *a*-axis and the polarization is set parallel to it, the intensity of the A_g^c mode becomes weaker than the background, thus we cannot know the RGF in that specific case (see Supplementary Fig. 4 and Supplementary Fig. 5. Additionally, we do not observe a dependence of the RGF with the thickness in the range we have studied.

Our observations reveal a discrepancy in the direction of the Raman mode shift compared to what is typically observed in other vdW materials[6,8,10–12,62,63]. Furthermore, a study conducted by Lv et al.[64] showed that the A_g^a Raman mode of MoO_3 redshifted with an increase of temperature. To shed light on this, we conducted theoretical calculations of Raman modes of MoO_3 under a uniaxial strain ranging from −1% (compression) to +1% (tension). Figure 5 illustrates the Raman modes of a MoO_3 sample subjected to strain from −1% to +1%, with a zoomed-in view (between two dashed vertical gray lines) of the shift of the A_g^c and A_g^a modes in the inset. Our calculations show, not only a consistent sign of wavenumber shift, but also the shift value for the A_g^a mode is larger than the one of the A_g^c mode with a RGF of $2 \pm 1\ cm^{-1}$/% for the A_g^c mode and $13 \pm 1\ cm^{-1}$/% for the A_g^a mode. For our theoretical calculations applying strain along one direction and measuring the Raman mode belonging to the perpendicular direction we observe a RGF of $1\ cm^{-1}$/% for the A_g^c mode, and $-4\ cm^{-1}$/% for the A_g^a mode. Thus, we can observe that the experimental results and the theoretical calculations agree not only in trend, but they also possess the same order of magnitude in the RGF.

To elucidate the distinctive blueshift observed in this material, when compared to most of the other vdW materials reported in the bibliography, we conducted a comprehensive review of the relevant literature. In a study focusing on the vibrational modes of multi-walled tungsten sulfide nanotubes, it was noted that the inter-layer vibration mode, denoted as A^1_g, exhibits sensitivity to variations in diameter and curvature-induced strain. The authors of this study postulated that an increase in the number of layers would intensify the van der Waals forces, thereby enhancing the stiffness of atomic vibrations and leading to a blueshift in the A^1_g mode[65]. This phenomenon mirrors observations in two-dimensional transition metal dichalcogenide films[66,67]. Furthermore, Li et al.[12] study Raman modes of black phosphorus with uniaxial strain, obtaining positive and negative shifts of the A^1_g and B_{2g} Raman modes depending on the direction of strain. The authors claim that this behavior corresponds to structural parameters. The applied strain, denoted as ε, comprises two components: longitudinal strain (ε_{long}) aligned with the direction of strain, and transverse strain (ε_{trans}), oriented perpendicular to it. These components are defined as $\varepsilon_{long} = \varepsilon$ and $\varepsilon_{trans} = -\nu \cdot \varepsilon_{long}$ where ν represents the Poisson's ratio. Notably, theoretical results from Huang et al.[68], emphasized that a compressive strain along the *b*-axis results in a slight expansion of the *a*-axis constant and a marginal contraction of the *c*-axis constant. Figure 2 in their study further illustrates that distortions along the *b* and *c* axes follow a similar trend, and opposite to the trend observed along the *a*-axis.

From these findings, we can conclude that the interplay between three orthogonal directions, the direction spanning the different layers in the *b*-axis, as well as the *a* and *c* axes, plays a pivotal role in accounting for the observed redshift (blueshift) of the A_g^a mode when strain is applied along the *c*-axis (*a*-axis). Moreover, this interplay elucidates the blueshift observed in the A_g^c mode when tensile strain is applied along both in-plane directions. Thus, these findings provide a strong framework for comprehending our own experimental results, although deeper research can be made in this direction in order to inspect carefully the specific modes and their behavior.

Moreover, we have carried out a cycling test to estimate the maximum number of stretching cycles. We have prepared a new MoO_3 sample of 28 nm thick on PC and we have performed 100 strains from 0% to 0.52% along the *a*-axis while we inspected the A_g^a mode, obtaining the RGF in some cycles. Supplementary Fig. 7 shows the RGF vs the number of cycles, where it is observed that the trend of the behavior is the same after that amount of cycles, although an increase of RGF absolute value is observed after a certain number of cycles, suggesting the preservation of the material properties.

Electrical characterization with strain

In addition to the phonon characterization of MoO_3, we have also studied the electrical piezoresponse of the material using the same steps in the growing method but using only mica muscovite as substrate. The reason of this decision is to yield wider and more uniform samples, which in turn enable us to interconnect the MoO_3 samples with the electrodes along both in-plane directions. The samples are transferred onto pre-patterned Au electrodes (50 nm thick and a separation distance of 20 μm), evaporated on a PC substrate using a deterministic transfer method, as shown in

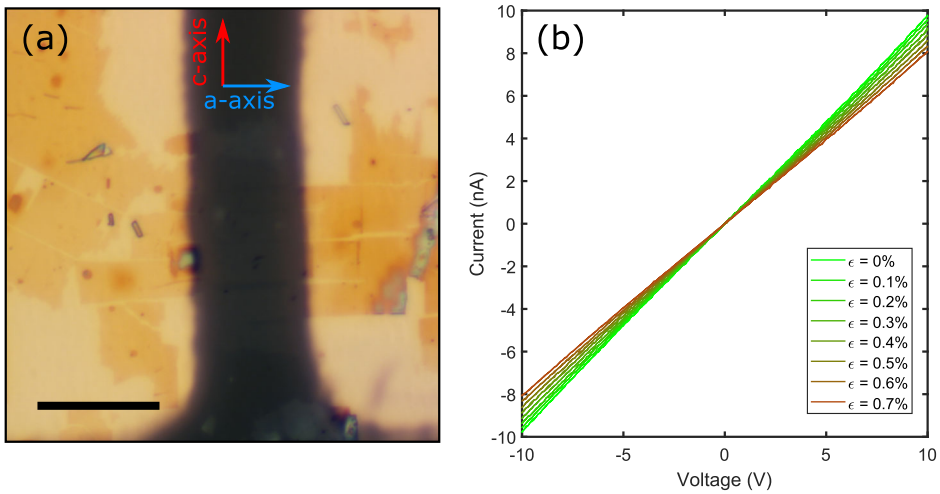

Fig. 6 Electrical measurements of MoO_3. a Optical microscope picture of a α-MoO_3 sample transferred onto Au electrodes evaporated on PC, aligning the *c*-axis parallel to the edge of the Au contacts, specified with arrows in the panel. Scale bar shown of 25 μm. **b** Current vs voltage measurements of the sample in (**a**) applying different values of strain, from 0% to 0.7% with a step of 0.1%.

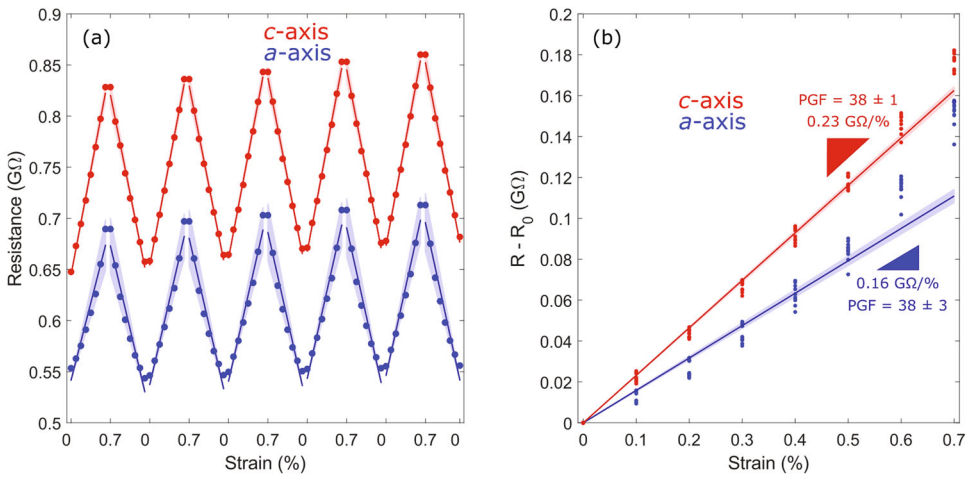

Fig. 7 Resistance shift of MoO_3 when applying strain along *a* and *c*-axes. a Change of resistance along five cycles of strain along the *c*-axis, in red, and *a*-axis, in blue; applying a tensile strain from 0% to 0.7% in each cycle. A linear fit in each cycle is applied and the uncertainty is calculated and shown as a shade of the linear fit. **b** Difference of resistance with the resistance at 0% of strain (R_0) versus the strain applied, a linear fit (from 0 to 0.5% of strain, due to the sublinear behavior of the experimental data for more strain) is used and plotted as a straight line, the uncertainty of the fit is then calculated and shown as a shade. The slope of the fit and the PGF are calculated and written in the plot.

the optical image of Fig. 6a. To accurately measure the electrical response, the PC substrate was placed in an automated three-point setup, which was described in detail in the ref. [69]. To ensure low-noise electrical measurements, the setup was placed inside a Faraday cage made of die-cast aluminum, as detailed in the Methods section (Supplementary Fig. 8). It protected the measurements from any electromagnetic perturbations that could have disrupted the results, leading to cleaner measurements. We conducted electrical measurements, at room temperature and ambient atmosphere, on the samples by connecting the gold electrodes to a sourcemeter (Keithley® 2450). A voltage of ±10 V was applied between the electrodes, resulting in a linear current in the order of nA. When a tensile strain was applied to the sample, the current decreased, as shown in Fig. 6b. This process is depicted through a cycle of strain from 0% to 0.7% with a step of 0.1%. The decrease in current when a tensile strain was applied highlights the responsiveness of the samples to different strains.

We have carried out electrical measurements applying strain along the *a*- and *c*-axes and we have obtained the resistance of the sample along five cycles of strain, showing reproducibility in the measurements, depicted in Fig. 7a. With the aid of the data in the panel (a) we can calculate the Piezoresistive Gauge Factor (PGF) using the following equation[70]:

$$PGF = \frac{\Delta R}{\varepsilon R_0} \quad (1)$$

Where ΔR is the change in resistance due to uniaxial strain, R_0 is the unstrained resistance and ε is the uniaxial strain applied. Figure 7b shows the difference of resistance when a strain is applied and when the sample is relaxed, obtaining the slope and the PGF belonging to each axis. We have used a linear fit in the region 0–0.5% of strain due to the sublinear behavior of the experimental data in the region 0.5–0.7% of strain. We have repeated these measurements with up to six samples, connecting three of them along *c*-axis and the rest along the *a*-axis. Surprisingly, we do not observe a substantial difference in the PGF between the two in-plane directions. Supplementary Table 2 shows in detailed the electrical values and physical dimensions of the samples we have used. We obtain an average PGF values of 38 ± 1 along the *c*-axis and 38 ± 3 along the *a*-axis.

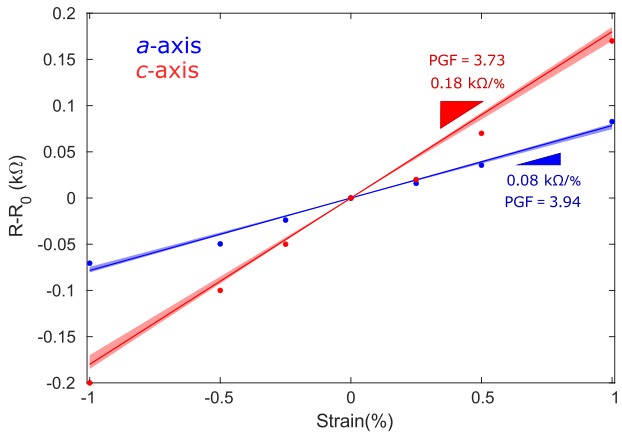

Fig. 8 Difference of resistance with the resistance at 0% of strain (R_0) versus the strain applied using theoretical calculations over a range from −1% to +1%. A linear fit of the data, in dark blue and red colors for *a*- and *c*-axes, respectively. Uncertainty region in shaded-area is shown. The slope and the PGF is obtained.

In comparison with the work of W. Xiaonan, et al.[71], we have obtained an opposite trend in the change of resistance when a strain is applied. In that work the authors synthesize α-MoO_3 of μm size by physical vapor deposition and perform the electrical measurements at a temperature of 200 °C under vacuum conditions. They claim that there is a piezoresistive effect occurring in their samples, which results from the strain-induced modulation of the band gap.

We have carried out theoretical calculations to obtain a change of conductance that agrees with our experimental results. In these calculations, the origin of the characteristic in the PGF is ruled by the following equation[70]:

$$PGF = GF_\rho + 1 + 2v, \tag{2}$$

where GF_ρ is the Gauge Factor of the resistivity, being this parameter intrinsic of the material, while the second part of the Eq. (2) refers to the Poisson's ratio, *v*. Usually the Poisson's ratio is relatively small when compared to the GF_ρ. Our numerical results, based on the solution of the Boltzmann transport equation for the electrons, in the linear response regime, shows that the electrical conductance shows little selectivity on the direction of the strain. Meaning that the piezoresistive gauge factor is essentially the same in both directions of the applied strain. This observation suggests that the dominant effect to determine the change in the conductance is the strain-induced variation of the band gap, while other factors (effective masses, relaxation times) are only weakly affected by the strain. Using these calculations, Fig. 8 displays the difference of the electrical resistance with the resistance at 0% of strain (R_0) of a MoO_3 device with similar dimensions to the samples that we experimentally tested. To perform these calculations, we employed a relaxation time of 100 fs. Furthermore, we estimated the theoretical PGF for this device, which turned out to be 3.94 along the *a*-axis and 3.73 along the *c*-axis. These values suggest that the electrical resistance exhibits behavior similar to our experimental results.

To further investigate in this topic, we have studied the dependence of the electrical resistance with the doping level (*N*), shown in the Supplementary Fig. 10, using the same the geometrical factors in Fig. 8. Thus, it can be observed that, by using the theoretical calculations, the electrical resistance increases when a tensile strain is applied and decreases with a compressive strain. Although there is a difference of three order of magnitude of the absolute values of the resistance with the experimental results, we observe the same trend of PGF along both axes, which agrees with our experimental results. The discrepancy between theory and experiment in the measured value of the resistance has indeed many origins and is difficult to assess.

On the one hand, our system is ideal -- we have not introduced any defects, impurities, or extra charges in our numerical description of the system. The introduction of a defect or impurity requires the use of large supercells. However, with these techniques, one is usually limited to high doping levels. An analysis based only on the results of these calculations would probably be inconclusive. The evaluation of the transport coefficient with the BTE relies on the Relaxation Time Approximation. We have tried a more refined estimate based on the Electron-Phonon averaged approximation (EPA)[72,73], which provides a strong renormalization of the relaxation time in other systems[74] and accurately reproduces a more refined approximation. Our EPA and RTA results agree (See Supplementary Fig. 11 in the Supplementary Information), suggesting that our estimate for the relaxation time at 100 fs is accurate for this material. On the other hand, it is well known that DFT might overestimate electrical conductivity. The reason for this behavior lies in the standard DFT approximations, which tend to delocalize the electronic wave function. This delocalization facilitates diffusion and electron transfer, thus reducing electrical resistance. However, our theoretical modeling reasonably reproduces the experimental gauge factors, thus suggesting that the effect leading to a larger electrical resistance does not strongly depend on strain. Further investigations can be realized in order to deeply investigate these phenomena.

In conclusion, we have investigated, the direction-dependent vibrational and electrical properties of α-MoO_3 when subjected to uniaxial strain. The findings of this study were supported by ab-initio calculations, and it was shown that the application of tensile strain along the same axis led to a blueshift in the wavenumber of two significant Raman modes, the A_g^c mode and the A_g^a mode, showing the opposite trend when compare with most of the other van der Waals materials studied. Moreover, we have observed an increase of the electrical resistance when a tensile strain is applied to the material, showing no difference of piezoresistive gauge factor along the two in-plane directions of α-MoO_3. This study increases our understanding of the mechanical, optical, and electrical anisotropic properties of this material.

METHODS

Growth and deposition

We have based our present grown procedure on a modification of the hot plate growth method developed by Molina-Mendoza et al.[59]. A Mo foil is placed on a hot-plate, preheated at 540 °C, and on top the substrate where the MoO_3 is going to be evaporated. We have used, as target substrates, a Si/SiO_2 wafer and a mica muscovite film for the Raman measurements and only the mica muscovite film for the electrical measurements. The Mo oxidizes and evaporates onto the substrate for 10–20 min. Once the growth of the crystals is finished, the MoO_3 is firstly exfoliated onto a polydimethylsiloxane (PDMS) (Gel-Film WF x4 6.0 mil, by Gelpak®) and then transferred onto a PC substrate using a deterministic transfer method[60,75].

Optical microscopy images

Optical microscopy images were acquired using a Motic BA310 MET-T microscope equipped with a 50 × 0.55 NA objective and an AMScope MU1803 CMOS Camera. More information about the set up can be found in the work of the ref. [76]

Strain dependent Raman linear polarized spectroscopy

Strain dependent Raman linear polarized spectroscopy: the disc-shape flexible substrate containing the desired flake on its center is loaded into the three-points bending system, depicted in Supplementary Fig. 1, in the Supp. Info., and the whole system is mounted under the objective of an confocal Raman microscopy system (MonoVista CRS+ from Spectroscopy & Imaging GmbH) using a 532 nm excitation laser with an incident power of 1.139 mW and a 50× objective with the integration time of 60 s. The assigned flake is centered with respect to the central pivot using microscope inspection with the camera of the Raman system.

Electrical measurements with strain

Electrical measurements were carried out with a Keithley® 2450 source measure unit. The MoO_3 devices were fixed on an automated home-made three-points bending setup, well-explained in this work[69], to conduct the well-defined tension deformations. The setup is placed inside a Faraday cage made of die-cast aluminum, in which has been included the BNC connections (see Supplementary Fig. 8). The electrical resistance of the device was determined by measuring current *vs*. voltage characteristics at various uniaxial strains. The Gauge Factor has been obtained using the Eq. (1), in which the uncertainty region has been derived using Propagation of error theory.

Numerical methods

We have performed ab-initio calculations to obtain the Raman spectra and the transport coefficients. For the Raman spectra we have used GPAW[77,78] in combination with ASE[79–81]. Starting with the available atomic configuration of bulk MoO_3, we have performed an energy minimization to obtain the equilibrium atomic positions. We have therefore modified the lattice constant in either the a or c direction to mimic the effect of external tensile strain. For each of the applied strain direction and magnitude, we have performed a new energy minimization to reduce the atomic residual forces. We then proceed to calculate the Raman spectra following the guidelines in the GPAW website. The code calculates the phonon structures and then the Raman tensor. For the electronic transport calculation, we have used Quantum Espresso in combination with Boltztrap2[82–84]. The former is an ab-initio plane wave code that calculates the electronic structure of the materials. BoltzTrap2 calculates the response coefficients through the numerical solution of the Boltzmann transport equation, in the constant relaxation time approximation. It uses for this calculation the electron bands obtained via Quantum Espresso.

For GPAW we used in plane-wave and LCAO mode. For the energy minimization steps, we used a uniform k-point mesh of $8 \times 8 \times 8$ in the first Brillouin zone. This is reduced to $5 \times 5 \times 5$ for the calculation of the Raman spectra for a supercell $2 \times 2 \times 2$. The convergence criterion is set on the density as a variation between loops of 10^{-7}.

For the Quantum Espresso calculations, we use ultra soft pseudopotentials in the generalized gradient approximation developed in the PBE scheme[85,86] with an energy cut-off of 40 Ry for the wave function and 400 Ry on the density. An $8 \times 8 \times 8$ uniform mesh is used for the energy minimization, while a uniform mesh of $10 \times 10 \times 10$ is used for the non-self-consistent calculation. The convergence is achieved when the energy changes are below 10^{-9} Ry.

In both GPAW and Quantum Espresso, we have included van der Walls corrections through the Grimme D2 approximation[87].

DATA AVAILABILITY

The data of this study are available from the corresponding author upon reasonable request.

Received: 14 July 2023; Accepted: 9 January 2024;
Published online: 24 January 2024

REFERENCES

1. Novoselov, K. S. Electric Field Effect in Atomically Thin Carbon Films. *Science* **306**, 666–669 (2004).
2. Bolotin, K. I. et al. Ultrahigh electron mobility in suspended graphene. *Solid State Commun.* **146**, 351–355 (2008).
3. Yang, S., Chen, Y. & Jiang, C. Strain engineering of two-dimensional materials: Methods, properties, and applications. *InfoMat* **3**, 397–420 (2021).
4. Bertolazzi, S., Brivio, J. & Kis, A. Stretching and Breaking of Ultrathin MoS2. *ACS Nano* **5**, 9703–9709 (2011).
5. Huang, M. et al. Phonon softening and crystallographic orientation of strained graphene studied by Raman spectroscopy. *Proc. Natl Acad. Sci.* **106**, 7304–7308 (2009).
6. Castellanos-Gomez, A. et al. Local Strain Engineering in Atomically Thin MoS 2. *Nano Lett.* **13**, 5361–5366 (2013).
7. Zhao, Q., Wang, T., Frisenda, R. & Castellanos-Gomez, A. Giant Piezoresistive Effect and Strong Bandgap Tunability in Ultrathin InSe upon Biaxial Strain. *Adv. Sci.* **7**, 2001645 (2020).
8. Li, H. et al. Stretching ReS2along different crystal directions: Anisotropic tuning of the vibrational and optical responses. *Appl. Phys. Lett.* **120**, 063101 (2022).
9. Li, H. et al. Strongly Anisotropic Strain-Tunability of Excitons in Exfoliated ZrSe 3. *Adv. Mater.* **34**, 2103571 (2022).
10. Androulidakis, C. H. et al. Strained hexagonal boron nitride: Phonon shift and Grüneisen parameter. *Phys. Rev. B* **97**, 241414 (2018).
11. Song, C. et al. Drastic enhancement of the Raman intensity in few-layer InSe by uniaxial strain. *Phys. Rev. B* **99**, 195414 (2019).
12. Li, Y. et al. Giant Anisotropic Raman Response of Encapsulated Ultrathin Black Phosphorus by Uniaxial Strain. *Adv. Funct. Mater.* **27**, 1600986 (2017).
13. Tan, C. K. et al. Raman studies of MoS 2 under strain at different uniaxial directions. *Vacuum* **153**, 274–276 (2018).
14. Li, Z. et al. Strain Releasing of Flexible 2D Electronics through van der Waals Sliding Contact. *ACS Nano* **16**, 13152–13159 (2022).
15. Iqbal, M. W., Shahzad, K., Akbar, R. & Hussain, G. A review on Raman finger prints of doping and strain effect in TMDCs. *Microelectron. Eng.* **219**, 111152 (2020).
16. Kim, J., Lee, J.-U. & Cheong, H. Polarized Raman spectroscopy for studying two-dimensional materials. *J. Phys. Condens. Matter* **32**, 343001 (2020).
17. Lee, J.-U., Kim, M. & Cheong, H. Raman Spectroscopic Studies on Two-Dimensional Materials. *Appl. Microsc.* **45**, 126–130 (2015).
18. Mohiuddin, T. M. G. et al. Uniaxial strain in graphene by Raman spectroscopy: *G* peak splitting, Grüneisen parameters, and sample orientation. *Phys. Rev. B* **79**, 205433 (2009).
19. Conley, H. J. et al. Bandgap Engineering of Strained Monolayer and Bilayer MoS 2. *Nano Lett.* **13**, 3626–3630 (2013).
20. Desai, S. B. et al. Strain-Induced Indirect to Direct Bandgap Transition in Multilayer WSe 2. *Nano Lett.* **14**, 4592–4597 (2014).
21. Huang, S. et al. Strain-tunable van der Waals interactions in few-layer black phosphorus. *Nat. Commun.* **10**, 2447 (2019).
22. Opra, D. P., Gnedenkov, S. V. & Sinebryukhov, S. L. Recent efforts in design of TiO2(B) anodes for high-rate lithium-ion batteries: A review. *J. Power Sources* **442**, 227225 (2019).
23. Noman, M. T., Ashraf, M. A. & Ali, A. Synthesis and applications of nano-TiO2: a review. *Environ. Sci. Pollut. Res.* **26**, 3262–3291 (2019).
24. Al-Rashedi, K., Farooqui, M., Mohsin, M. & Rabbani, G. METAL OXIDE THIN FILMS: A MINI REVIEW. *J. Adv. Sci. Res.* **7**, 1–8 (2016).
25. Kumar, R., Kumar, G., Al-Dossary, O. & Umar, A. ZnO nanostructured thin films: Depositions, properties and applications—A review. *Mater. Express* **5**, 3–23 (2015).
26. Weng, W. Y., Chang, S. J., Hsu, C. L. & Hsueh, T. J. A ZnO-Nanowire Phototransistor Prepared on Glass Substrates. *ACS Appl. Mater. Interfaces* **3**, 162–166 (2011).
27. Timmerman, M. A., Xia, R., Le, P. T. P., Wang, Y. & Elshof, J. E. Metal Oxide Nanosheets as 2D Building Blocks for the Design of Novel Materials. *Chem.A Eur. J.* **26**, 9084–9098 (2020).
28. Xiong, P., Ma, R., Sakai, N. & Sasaki, T. Genuine Unilamellar Metal Oxide Nanosheets Confined in a Superlattice-like Structure for Superior Energy Storage. *ACS Nano* **12**, 1768–1777 (2018).
29. Zhang, X. et al. Rapid hydrothermal synthesis of hierarchical nanostructures assembled from ultrathin birnessite-type MnO2 nanosheets for supercapacitor applications. *Electrochim. Acta* **89**, 523–529 (2013).
30. Park, J. W., Kang, B. H. & Kim, H. J. A Review of Low-Temperature Solution-Processed Metal Oxide Thin-Film Transistors for Flexible Electronics. *Adv. Funct. Mater.* **30**, 1904632 (2020).

31. Frisenda, R., Niu, Y., Gant, P., Muñoz, M. & Castellanos-Gomez, A. Naturally occurring van der Waals materials. *NPJ 2D Mater. Appl* **4**, 38 (2020).
32. Bouzidi, A. et al. Effect of substrate temperature on the structural and optical properties of MoO3 thin films prepared by spray pyrolysis technique. *Mater. Sci. Eng. B* **97**, 5–8 (2003).
33. Bruce King, R. *Encyclopedia of inorganic chemistry*, Wiley (2006).
34. Zhang, W.-B., Qu, Q. & Lai, K. High-Mobility Transport Anisotropy in Few-Layer MoO_3 and Its Origin. *ACS Appl. Mater. Interfaces* **9**, 1702–1709 (2017).
35. Zheng, B., Wang, Z., Chen, Y., Zhang, W. & Li, X. Centimeter-sized 2D α-MoO_3 single crystal: growth, Raman anisotropy, and optoelectronic properties. *2d Mater.* **5**, 045011 (2018).
36. Sitepu, H. Texture and structural refinement using neutron diffraction data from molybdite (MoO_3) and calcite ($CaCO_3$) powders and a Ni-rich $Ni_{50.7}Ti_{49.30}$ alloy. *Powder Diffr.* **24**, 315–326 (2009).
37. Py, M. A., Schmid, P. H. E. & Vallin, J. T. Raman scattering and structural properties of MoO3. *Il Nuovo Cim. B Ser. 11* **38**, 271–279 (1977).
38. Puebla, S. et al. In-plane anisotropic optical and mechanical properties of two-dimensional MoO_3. *NPJ 2D Mater. Appl* **5**, 37 (2021).
39. Mai, L. Q. et al. Lithiated MoO3 Nanobelts with Greatly Improved Performance for Lithium Batteries. *Adv. Mater.* **19**, 3712–3716 (2007).
40. Lee, S.-H. et al. Reversible Lithium-Ion Insertion in Molybdenum Oxide Nanoparticles. *Adv. Mater.* **20**, 3627–3632 (2008).
41. Julien, C. M. Lithium intercalated compounds. *Mater. Sci. Eng. R. Rep.* **40**, 47–102 (2003).
42. Wang, C., Irfan, I., Liu, X. & Gao, Y. Role of molybdenum oxide for organic electronics: Surface analytical studies. *J. Vac. Sci. Technol. B Nanotechnol. Microelectron. Mater. Process. Meas. Phenom.* **32**, 040801 (2014).
43. Hu, B., Mai, L., Chen, W. & Yang, F. From MoO3 Nanobelts to MoO2 Nanorods: Structure Transformation and Electrical Transport. *ACS Nano* **3**, 478–482 (2009).
44. Cyril Robinson Azariah, J. et al. Pulsed Laser Deposited Molybdenum Oxides (MoO3 & MoO2) Thin Films for Nanoelectronics Device Application. In: *2018 4th International Conference on Devices, Circuits and Systems (ICDCS)* 42–47 (IEEE, 2018). https://doi.org/10.1109/ICDCSyst.2018.8605070.
45. Rahman, F. et al. Dual Selective Gas Sensing Characteristics of 2D α-MoO 3– x via a Facile Transfer Process. *ACS Appl. Mater. Interfaces* **11**, 40189–40195 (2019).
46. Korotcenkov, G. *Metal Oxides in Supercapacitors* (Elsevier, 2017).
47. Wang, Y. et al. Mesoporous Transition Metal Oxides for Supercapacitors. *Nanomaterials* **5**, 1667–1689 (2015).
48. Cho, E., Cha, S., Kim, Y. & Kim, C. Transparent and flexible electrode composed of a graphene multilayer interlayer-doped with MoO3. *Org. Electron* **77**, 105437 (2020).
49. Han, Y. C., Lim, M. S., Park, J. H. & Choi, K. C. ITO-free flexible organic light-emitting diode using ZnS/Ag/MoO3 anode incorporating a quasi-perfect Ag thin film. *Org. Electron* **14**, 3437–3443 (2013).
50. Tan, Z.-H., Yin, X.-B. & Guo, X. One-dimensional memristive device based on MoO3 nanobelt. *Appl Phys. Lett.* **106**, 023503 (2015).
51. Ma, W. et al. In-plane anisotropic and ultra-low-loss polaritons in a natural van der Waals crystal. *Nature* **562**, 557–562 (2018).
52. Zheng, Z. et al. A mid-infrared biaxial hyperbolic van der Waals crystal. *Sci. Adv.* **5**, eaav8690 (2019).
53. Chen, M. et al. Configurable phonon polaritons in twisted α-MoO_3. *Nat. Mater.* **19**, 1307–1311 (2020).
54. Zheng, Z. et al. Phonon Polaritons in Twisted Double-Layers of Hyperbolic van der Waals Crystals. *Nano Lett.* **20**, 5301–5308 (2020).
55. Hu, Y. et al. Near-field radiative modulator driven by anisotropic hyperbolic polaritons in biaxial hyperbolic materials. *J. Quant. Spectrosc. Radiat. Transf.* **296**, 108468 (2023).
56. Zhang, Y. et al. Tailoring the Phonon Polaritons in *α* -MoO_3 via Proton Irradiation. *Adv. Opt. Mater.* **11**, 2300180 (2023).
57. Zeng, Y. et al. Optical nanoimaging of highly-confined phonon polaritons in atomically-thin nanoribbons of α-MoO_3. *Opt. Express* **31**, 28010 (2023).
58. Carrascoso, F., Li, H., Frisenda, R. & Castellanos-Gomez, A. Strain engineering in single-, bi- and tri-layer MoS_2, $MoSe_2$, WS_2 and WSe_2. *Nano Res.* **14**, 1698–1703 (2021).
59. Molina-Mendoza, A. J. et al. Centimeter-Scale Synthesis of Ultrathin Layered MoO_3 by van der Waals Epitaxy. *Chem. Mater.* **28**, 4042–4051 (2016).
60. Castellanos-Gomez, A. et al. Deterministic transfer of two-dimensional materials by all-dry viscoelastic stamping. *2d Mater.* **1**, 011002 (2014).
61. Carrascoso, F., Frisenda, R. & Castellanos-Gomez, A. Biaxial versus uniaxial strain tuning of single-layer MoS2. *Nano. Mater. Sci.* **4**, 44–51 (2022).
62. Blundo, E., Cappelluti, E., Felici, M., Pettinari, G. & Polimeni, A. Strain-tuning of the electronic, optical, and vibrational properties of two-dimensional crystals. *Appl Phys. Rev.* **8**, 021318 (2021).
63. Wang, G. et al. Out-of-Plane Deformations Determined Mechanics of Vanadium Disulfide (VS_2) Sheets. *ACS Appl Mater. Interfaces* **13**, 3040–3050 (2021).
64. Lv, X. et al. In-situ investigation on the thermal decomposition of van der Waals MoO3. *Chem. Phys. Lett.* **779**, 138840 (2021).
65. Wang, X. H., Zheng, C. C. & Ning, J. Q. Influence of curvature strain and Van der Waals force on the inter-layer vibration mode of WS2 nanotubes: A confocal micro-Raman spectroscopic study. *Sci. Rep.* **6**, 33091 (2016).
66. Berkdemir, A. et al. Identification of individual and few layers of WS2 using Raman Spectroscopy. *Sci. Rep.* **3**, 1755 (2013).
67. Li, H. et al. From Bulk to Monolayer MoS_2: Evolution of Raman Scattering. *Adv. Funct. Mater.* **22**, 1385–1390 (2012).
68. Huang, P.-R., He, Y., Cao, C. & Lu, Z.-H. Impact of lattice distortion and electron doping on α-MoO_3 electronic structure. *Sci. Rep.* **4**, 7131 (2015).
69. Çakıroğlu, O., Island, J. O., Xie, Y., Frisenda, R. & Castellanos-Gomez, A. An Automated System for Strain Engineering and Straintronics of 2D Materials. *Adv. Mater. Technol.* **8**, 2201091 (2022).
70. Beckwith, Thomas G., N. Lewis Buck, R. D. M. *Mechanical Measurements* (Wesley Publishing Co, 1982).
71. Wen, X., Yang, W., Ding, Y., Niu, S. & Wang, Z. L. Piezoresistive effect in MoO3 nanobelts and its application in strain-enhanced oxygen sensors. *Nano Res* **7**, 180–189 (2014).
72. Samsonidze, G. & Kozinsky, B. Accelerated Screening of Thermoelectric Materials by First-Principles Computations of Electron–Phonon Scattering. *Adv. Energy Mater.* **8**, 1800246 (2018).
73. Cepellotti, A., Coulter, J., Johansson, A., Fedorova, N. S. & Kozinsky, B. Phoebe: a high-performance framework for solving phonon and electron Boltzmann transport equations. *J. Phys. Mater.* **5**, 035003 (2022).
74. Biele, R. & D'Agosta, R. Transport coefficients of layered <math> <msub> <mrow> <mi>TiS</mi> </mrow> <mn>3</mn> </msub> </math>. *Phys. Rev. Mater.* **6**, 014004 (2022).
75. Zhao, Q., Wang, T., Ryu, Y. K., Frisenda, R. & Castellanos-Gomez, A. An inexpensive system for the deterministic transfer of 2D materials. *J. Phys.: Mater.* **3**, 016001 (2020).
76. Frisenda, R. et al. Micro-reflectance and transmittance spectroscopy: a versatile and powerful tool to characterize 2D materials. *J. Phys. D. Appl. Phys.* **50**, 074002 (2017).
77. Mortensen, J. J., Hansen, L. B. & Jacobsen, K. W. Real-space grid implementation of the projector augmented wave method. *Phys. Rev. B* **71**, 035109 (2005).
78. Enkovaara, J. et al. Electronic structure calculations with GPAW: a real-space implementation of the projector augmented-wave method. *J. Phys. Condens. Matter* **22**, 253202 (2010).
79. Hjorth Larsen, A. et al. The atomic simulation environment—a Python library for working with atoms. *J. Phys. Condens. Matter* **29**, 273002 (2017).
80. Lehtola, S., Steigemann, C., Oliveira, M. J. T. & Marques, M. A. L. Recent developments in libxc — A comprehensive library of functionals for density functional theory. *SoftwareX* **7**, 1–5 (2018).
81. Larsen, A. H., Vanin, M., Mortensen, J. J., Thygesen, K. S. & Jacobsen, K. W. Localized atomic basis set in the projector augmented wave method. *Phys. Rev. B Condens. Matter. Mater. Phys.* **80**, 195112 (2009).
82. Giannozzi, P. et al. QUANTUM ESPRESSO: a modular and open-source software project for quantum simulations of materials. *J. Phys. Condens. Matter* **21**, 395502 (2009).
83. Madsen, G. K. H., Carrete, J. & Verstraete, M. J. BoltzTraP2, a program for interpolating band structures and calculating semi-classical transport coefficients. *Comput. Phys. Commun.* **231**, 140–145 (2018).
84. Madsen, G. K. H. & Singh, D. J. BoltzTraP. A code for calculating band-structure dependent quantities. *Comput. Phys. Commun.* **175**, 67–71 (2006).
85. Kohn, W. & Sham, L. J. Self-consistent equations including exchange and correlation effects. *Phys. Rev.* **140**, A1133 (1965).
86. Perdew, J. P., Burke, K. & Ernzerhof, M. Generalized Gradient Approximation Made Simple. *Phys. Rev. Lett.* **77**, 3865 (1996).
87. Grimme, S. Semiempirical GGA-type density functional constructed with a long-range dispersion correction. *J. Comput. Chem.* **27**, 1787–1799 (2006).

ACKNOWLEDGEMENTS

The authors acknowledge funding from the European Research Council (ERC) through the project 2D-TOPSENSE (GA 755655), the European Union's Horizon 2020 research and innovation program under the grant agreement 956813 (2Exciting), the EU FLAG-ERA through the project To2Dox (PCI2019-111893-2), Comunidad de Madrid through the project CAIRO-CM project (Y2020/NMT-6661), and the Spanish Ministry of Science and Innovation through the projects PID2020-115566RB-I00 and fellowship PRE2018-084818. R.D'A. acknowledges support from the Grant No. IT1453-22 "Grupos Consolidados UPV/EHU del Gobierno Vasco" and Grant PID2020-112811GB-I00 funded by MCIN/AEI/10.13039/501100011033. H.L. acknowledges the grant from China Scholarship Council (CSC) under no. 201907040070.

AUTHOR CONTRIBUTIONS

S.P. and H.L. fabricated the MoO_3 samples and performed the angle-resolved Raman measurements with strain. S.P. and O.Ç. performed the electrical measurements with strain. R.D'A. performed the theoretical calculations. C.M. and A.C.-G. supervised and designed the experiments. E.S. carried out the AFM measurements. S.P., C.M. and A.C.-G. drafted the firsts version of the manuscript. All authors contributed to writing the final version of the manuscript.

COMPETING INTERESTS

The authors declare no competing interests.

ADDITIONAL INFORMATION

Supplementary information The online version contains supplementary material available at https://doi.org/10.1038/s41699-024-00442-3.

Correspondence and requests for materials should be addressed to Sergio Puebla, Roberto D'Agosta or Andres Castellanos-Gomez.